Journal of Power Sources 195 (2010) 3266–3274

Contents lists available at ScienceDirect

Journal of Power Sources

journal homepage: www.elsevier.com/locate/jpowsour

Enhanced hydrogen sorption kinetics of $Mg_{50}Ni$–$LiBH_4$ composite by $CeCl_3$ addition

F.C. Gennari, J.A. Puszkiel*

Consejo Nacional de Investigaciones Científicas y Tecnológicas (CONICET), Instituto Balseiro (UNCuyo), Centro Atómico Bariloche (CNEA), Instituto Balseiro (UNCuyo), Av. Bustillo km 9.5, R8402AGP, S. C. Bariloche, Argentina

ARTICLE INFO

Article history:
Received 30 October 2009
Received in revised form 1 December 2009
Accepted 2 December 2009
Available online 5 December 2009

Keywords:
Hydrogen storage
Lithium borohydride
Magnesium
Catalyst
Mechanical milling

ABSTRACT

$Mg_{50}Ni$–$LiBH_4$ and $Mg_{50}Ni$–$LiBH_4$–$CeCl_3$ composites have been prepared by short times of ball milling under argon atmosphere. Combination of HP–DSC and volumetric techniques show that $Mg_{50}Ni$–$LiBH_4$–$CeCl_3$ composite not only uptakes hydrogen faster than $Mg_{50}Ni$–$LiBH_4$, but also releases hydrogen at a lower temperature (225 °C). The presence of $CeCl_3$ has a catalytic role, but it does not modify the thermodynamic properties of the composite which corresponds to MgH_2. Experimental studies on the hydriding/dehydriding mechanisms demonstrate that $LiBH_4$ and Ni lead to the formation of $MgNi_3B_2$ in both composites. In addition, XRD/DSC analysis and thermodynamic calculations demonstrate that the addition of $CeCl_3$ accounts for the enhancement of the hydrogen absorption/desorption kinetics through the interaction with $LiBH_4$. The in situ formation and subsequent decomposition of $Ce(BH_4)_3$ provides a uniform distribution of nanosize CeB_4 compound, which plays an important role in improving the kinetic properties of MgH_2.

© 2009 Elsevier B.V. All rights reserved.

1. Introduction

Hydrogen has attracted significant interest as an ideal energy carrier for mobile applications. However, the safe and efficient storage of hydrogen poses an engineering challenge for clean and environmentally friendly transportation. Solid-state media are an advantageous alternative for reversible and safe storage compared either with liquid hydrogen tanks or compressed hydrogen gas. High gravimetric and volumetric hydrogen capacities as well as effective thermodynamic stability and fast kinetics are among the stringent limits that a viable on-board solid hydrogen carrier must meet [1].

Various hydrogen storage materials, such as metal hydrides, nanocarbon materials, complex metal hydrides (alanates AlH_4^-, amides NH_2^- and borohydrides BH_4^-) and metal-organic frameworks (MOFs), have been investigated. Among them, magnesium hydride is still one of the most attractive options since it can reversibly store 7.6 wt% H and it is cheap and widely available [2–5]. Unfortunately, the application of MgH_2 is primarily precluded by its high desorption temperature and slow absorption/desorption kinetics below 300 °C, attributed to the strong ionic bond between Mg and H [6]. Different techniques have been applied to overcome these difficulties: the development of ball milling procedures, the addition of catalysts and the combination with complex hydrides [7–27]. The ball milling technique allows the production of nanocrystalline materials with homogeneous composition and refined microstructure [7]. One approach, which consists on adding mainly 3d transition metals and their oxides/halides with catalytic effect on MgH_2, has been used to prepare Mg-based composites by mechanical milling [8–24]. Another approach, instead, is the combination of MgH_2 with small amounts of $LiBH_4$ resulting in a noticeable enhancement of the hydrogen capacity and sorption kinetics of the obtained materials [25–27]. Johnson et al. [25] have reported that MgH_2 with modest amounts of $LiBH_4$ absorbs 6.0 wt% H at 300 °C under 1 MPa in about 40 min. Moreover, Mao et al. [26] have observed that $LiBH_4$/Mg (mass ratio 1:4) composite can uptake 2.6, 6.7 and 7.2 wt% of hydrogen within 60 min under 3 MPa, at 200, 250 and 300 °C, respectively. We have found [27] that the capacity and kinetics of metal-doped Mg materials ($Mg_{50}Ni$ and $Mg_{15}Fe$) can be noticeably enhanced by the addition of a small quantity of $LiBH_4$. Reversible hydrogen storage capacities of about 7.0 wt% H at 300 °C under 2.5 MPa in just 300 s have been achieved with $Mg_{50}Ni$–10 mol%$LiBH_4$ composite. This result has shown that $LiBH_4$ is an excellent additive for the milling process as it makes possible the further agglomerate and crystallite size reduction of Mg, increasing its surface area without apparent chemical reaction. Furthermore, its presence during hydrogen cycling leads to the formation of the $MgNi_3B_2$ phase which does not absorb hydrogen but improves the absorption kinetics of $Mg_{50}Ni$–$LiBH_4$ in comparison to $Mg_{15}Fe$–$LiBH_4$.

In this work, we study the microstructure and hydrogen release/uptake properties of ball-milled $Mg_{50}Ni$–$LiBH_4$ composites

* Corresponding author. Tel.: +54 02944 44 5197/18; fax: +54 2944 44 5190.
E-mail address: jpuszkiel@cab.cnea.gov.ar (J.A. Puszkiel).

0378-7753/$ – see front matter © 2009 Elsevier B.V. All rights reserved.
doi:10.1016/j.jpowsour.2009.12.006

with and without the addition of $CeCl_3$. The microstructural characteristics of the nanocomposites were examined by powder X-ray diffraction (PXRD) and scanning electron microscopy (SEM). Their hydrogen sorption properties were investigated using differential scanning calorimetry under argon and high hydrogen pressure atmosphere (DSC and HP-DSC), and Sieverts techniques. The interactions between Mg, Ni and $LiBH_4$, and the role of $CeCl_3$ were also analyzed.

2. Experimental methods

2.1. Sample preparation

Magnesium based composites were prepared by ball milling under argon atmosphere using a planetary mill (Fritsch P-6). Mg (purchased from Riedel-de Haën; purity > 99.9%) and Ni (purchased from Sigma–Aldrich; purity > 99.9%) powders in a stoichiometric proportion of 50:1($Mg_{50}Ni$) were milled during 10 h. Subsequently, 10 mol% of $LiBH_4$ (purchased from Sigma–Aldrich, purity ≥90%) and 0.2 mol% of anhydrous $CeCl_3$ (purchased from Sigma–Aldrich; purity > 99.9%) were added to $Mg_{50}Ni$ via 2 additional hours of ball milling to obtain $Mg_{50}Ni$–10 mol%$LiBH_4$ and $Mg_{50}Ni$–10 mol%$LiBH_4$–0.2$CeCl_3$. Samples containing Mg–10 mol%$LiBH_4$–0.2$CeCl_3$ and Mg–50 mol%$LiBH_4$–1 mol%$CeCl_3$ were also prepared to clarify the hydrogen sorption mechanism and the occurring interactions among the constitutive elements of the nanocomposites materials under study. These additional samples were obtained by adding the corresponding amounts of $LiBH_4$ and $CeCl_3$ to as-milled Mg through 2 h of ball milling. All samples were milled using a sealed hardened steel container (80 cm^3), a ball to sample mass ratio of 40:1 (sample mass: 2–3 g) and a disc speed of 400 rpm. In order to prevent all samples from undergoing oxidation and/or hydroxide formation, they were stored and handled in a MBraum Unilab 1200 argon-filled glove box with oxygen and moisture levels lower than 1 ppm. The prepared $Mg_{50}Ni$–10 mol%$LiBH_4$, $Mg_{50}Ni$–10 mol%$LiBH_4$–0.2 mol%$CeCl_3$, Mg–10 mol%$LiBH_4$–0.2$CeCl_3$ and Mg–50 mol%$LiBH_4$–1 mol%$CeCl_3$ composites are hereafter indicated as: Mg–50Li–1Ce, Mg–Ni–10Li, Mg–Ni–10Li–0.2Ce and Mg–10Li–0.2Ce.

2.2. Thermodynamic and kinetic measurements

Static pressure-composition isotherms (PCI) and isothermal hydrogen sorption kinetics were examined using a modified Sieverts-type device coupled with a mass flow controller [28]. Absorption–desorption PCIs were measured in the temperature range of 250–400 °C, heating up each sample to the reaction temperature under vacuum and keeping them at this temperature for 30 min before the measurement. The equilibrium hydrogen reversible capacities were determined from the plateau widths and the equilibrium plateau pressures calculated from the obtained PCI curves as an average of the experimental points in the plateau region, taking into account the error propagation theory. Using the calculated equilibrium pressures the absorption/desorption van't Hoff plots were constructed and the hydrogenation/dehydrogenation enthalpy and entropy calculated. Hydrogen absorption/desorption rates were evaluated between 225 and 350 °C under 2.5 MPa. All the kinetic measurements were carried out after activation of the materials reaching stable capacities and rates through successive absorption/desorption cycles at 350 °C and 2.5 MPa.

2.3. Characterization

Morphological and microstructural characterizations were performed via scanning electron microscopy with an energy-dispersive X-ray spectrometer analyzer (SEM-EDS 515, Philips Electronic Instruments). For the SEM observations and EDS analyses, samples of the synthesized powders were dispersed on stick-mounted holders and introduced into hermetic plastic recipients in the argon-filled glove box to further minimize the material's surface exposure to oxygen and humidity. The values of Mg, Ni, Ce and Cl atomic percentages of the corresponding composites after hydrogen cycling were estimated by EDS as an average of five measurements, one taken from a general sector and four taken from different sectors of the powders dispersed on the stick.

The structural modifications rendered by the milling and hydriding/dehydriding processes were examined by powder X-ray diffraction (PXRD) analysis (Philips PW 1710/01 Instruments) with Cu Kα radiation (λ = 1.5418 Å, graphite monochromator, operated at 40 kV and 30 mA). During the PXRD data collection all the samples were maintained under Ar atmosphere using a tightly sealed sample holder to prevent the reaction between samples and air. Crystallite size changes were estimated from diffraction peaks by Scherrer equation.

The thermal behavior of the samples under argon atmosphere was studied by DSC (DSC, TA Instruments 2910 calorimeter) using 5 °C min^{-1} of heating rate and 122 ml min^{-1} argon flow rate. High-pressure differential scanning calorimeter (HP-DSC, TA Instrument 2910 calorimeter) was used to investigate the non-isothermal hydriding/dehydriding behavior under hydrogen atmosphere (2.0 or 2.5 MPa H_2 for absorption and vacuum for desorption). For DSC and HP-DSC thermal analyses about 10 mg of samples were loaded into hermetically closed aluminum capsules in the above mentioned MBraum Unilab argon-filled glove box. Temperature ramp experiments were performed in the above mentioned Sieverts-type device (Section 2.2).

2.4. Thermodynamic calculations

The HSC Chemistry software [29] was used to assess the reactivity of Mg–Li–Ce system under vacuum and hydrogen atmosphere in equilibrium conditions. The most favorable reactions were identified through a combination of Gibbs minimization equilibrium with selected solid and gas species. The obtained predictions represent ideal chemical phase equilibria and are used to predict possible solid products, in particular those involving Ce.

3. Results and discussion

3.1. Structural and microstructural characterization

Fig. 1 shows the powder XRD patterns of the Mg–Ni–10Li–0.2Ce sample (a) after milling, (b) after hydrogen absorption and (c) after hydrogen desorption at 300 °C. The PXRD pattern of the sample after milling shows the presence of Mg, Ni, $LiBH_4$ and $CeCl_3$, which indicates that the obtained material is a physical mixture of the starting materials. In the sample after hydrogen absorption MgH_2 and $MgNi_3B_2$ are detected. Mg stems from MgH_2 decomposition and $MgNi_3B_2$ remains as secondary phase after hydrogen desorption. Similar results were obtained with the Mg–Ni–10Li, i.e. a physical mixture of Mg, Ni and $LiBH_4$ after milling as well as the $MgNi_3B_2$ after hydrogen absorption/desorption [27]. Up to this point the presence of $CeCl_3$ would not lead to the formation of a new phase detectable using PXRD.

The grain sizes of Mg before and after hydrogen cycling were calculated from the PXRD patterns. It was found that the Mg–Ni–10Li and Mg–Ni–10Li–0.2Ce composites milled for 2 h present Mg grain sizes of 20 and 25 nm, respectively. After hydrogen cycling at 350 °C the grain size of Mg increases and reaches 40 nm. Then, the difference between the grain size of Mg before and after hydrogen cycling

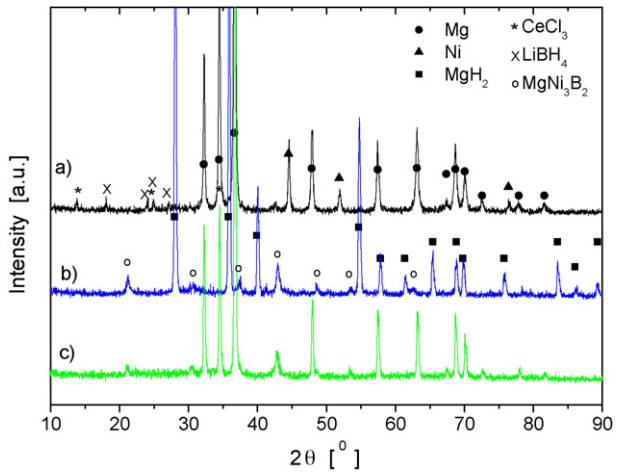

Fig. 1. Powder X-ray diffraction patterns for Mg–Ni–10Li–0.2Ce (a) after milling; (b) after hydrogen absorption at 300 °C under 2.5 MPa and (c) after hydrogen desorption at 300 °C under vacuum.

is not relevant. These results show that the grain size refinement of Mg is practically the same for both composites, maintaining the nanometric range after successive hydrogen cycles.

Fig. 2 shows the agglomerate size distribution and the particle morphology of as-milled Mg–Ni–10Li and Mg–Ni–10Li–0.2Ce (Fig. 2(A) and (C)) and after hydrogen cycling (Fig. 2(B) and (D)). After milling, both composites exhibit practically the same agglomerate size distribution (below 30 μm) and granular shape morphology with cracks on the surface (inset plots). As previously reported [27], the agglomerate size of Mg doped with Ni ($Mg_{50}Ni$) was noticeably reduced from 50 to 150 μm to below 30 μm when $LiBH_4$ was added (Mg–Ni–10Li). This suggests that $LiBH_4$ facilitates the ball milling of ductile Mg. After hydriding/dehydriding most of the agglomerates were pulverized into small and like coral clusters with sizes below 2 μm as a consequence of the hydrogen penetration into the material. EDS analyses (see Fig. 2(B) and 2(D)) taken from different sectors of the samples (see Section 2.3) after hydrogen cycling provide the atomic content of the corresponding elements in the composites. For the Mg–Ni–10Li composite, the amounts of Mg and Ni are 98.7% and 1.3%, respectively. In the case of Mg–Ni–10Li–0.2Ce, the amounts of Mg, Ni, Cl and Ce are 96.8%, 2.0%, 1.0% and 0.3%, respectively.

These experimental results reveal that Mg–Ni–10Li and Mg–Ni–10Li–0.2Ce composites do not present any relevant difference in their morphological and microstructural characteristics. Furthermore, the EDS analyses show that for both composites Ce, Ni and Cl are well distributed on the surface of MgH_2, maintaining the starting atomic percentages after hydrogen cycling.

3.2. Thermodynamic properties

Absorption/desorption PCIs were carried out to characterize the behavior of the Mg–Ni–10Li and Mg–Ni–10Li–0.2Ce composites in the equilibrium conditions. Fig. 3 shows the (A) PCIs at 300 and 350 °C of Mg–Ni–10Li and Mg–Ni–10Li–0.2Ce, and (B) desorption van't Hoff plots of Mg–Ni, Mg–Ni–10Li and Mg–Ni–10Li–0.2Ce composites. The obtained isotherms are qualitatively similar containing only one plateau over the whole range of temperature ascribed to MgH_2. At 300 and 350 °C the hydrogen capacities reached the equilibrium conditions are about 7.0 wt% H and 6.7 wt% H for Mg–Ni–10Li and Mg–Ni–10Li–0.2Ce composites. The Mg–Ni–10Li–0.2Ce composite presents flattened plateaus with smaller hysteresis and lower absorption equilibrium pressure than Mg–Ni–10Li, but practically the same desorption equilibrium pressures.

A noticeable increase of the equilibrium pressure of Mg–Ni–10Li and Mg–Ni–10Li–0.2Ce composites in relation to Mg–Ni is revealed from the absorption (not shown)/desorption van't Hoff. However, this increase is small in a factor less than 1.5 for Mg–Ni–10Li and 1.1 for Mg–Ni–10Li–0.2Ce to cause a change in the thermodynamic behavior of the composites [30]. Moreover, relevant differences among the composites and MgH_2 [31,32] do not emerge from the absorption/desorption enthalpies shown in Table 1. Therefore, the thermodynamic of the composites correspond to MgH_2.

3.3. Kinetic behavior

Studies on the reactivity with hydrogen of the as-milled Mg–Ni–10Li and Mg–Ni–10Li–0.2Ce composites using HP-DSC

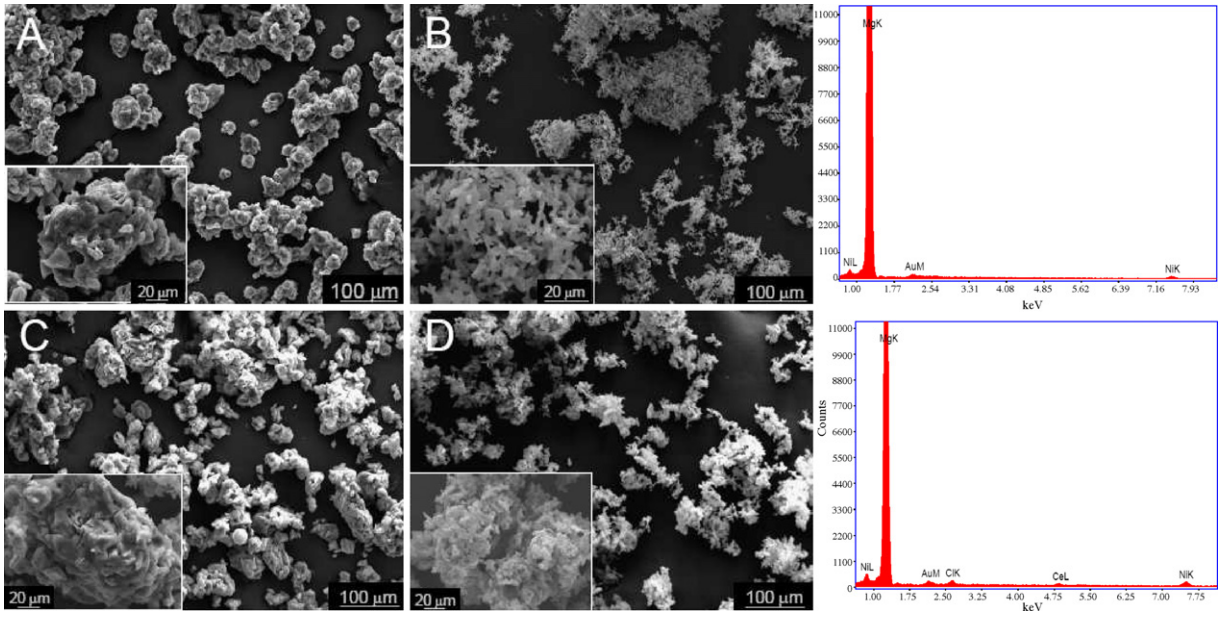

Fig. 2. SEM morphologies of (A) Mg–Ni–10Li after milling, (B) Mg–Ni–10Li after hydrogen cycling with EDS analysis from a general sector, (C) Mg–Ni–10Li–0.2Ce after milling and (D) Mg–Ni–10Li–0.2Ce after hydrogen cycling with EDS analysis from a general sector. (The presence of Au in the EDS analyses is owing to the Au coating on the surface of the sample needed to have an electrically conductive surface.)

Table 1
Formation and decomposition enthalpies and entropies obtained from the van't Hoff plots.

Composition	Absorption		Desorption	
	ΔH (kJ mol^{-1} H_2)	ΔS (J mol^{-1} H_2 K^{-1})	ΔH (kJ mol^{-1} H_2)	ΔS (J mol^{-1} H_2 K^{-1})
Mg–Ni[a]	−72	−132	−72	−132
Mg–Ni–10Li[a]	−67 ± 1	−126 ± 2	−77 ± 2	−140 ± 3
Mg–Ni–10Li–0.2Ce	−68 ± 1	−126 ± 2	−73 ± 2	−133 ± 4
MgH_2[b,c]	−70[b]	−126[b]	−74.4[c]	−135[c]

[a] Ref. [27].
[b] Ref. [31].
[c] Ref. [32].

non-isothermal measurements are shown in Fig. 4(A) and (B). As seen in Fig. 4(A), the Mg–Ni–10Li–0.2Ce composite starts to absorb hydrogen at a lower temperature (150 °C) than the Mg–Ni–10Li composite (250 °C). Fig. 4(B) shows that the hydrogen release under vacuum after the first cycle also occurs at a lower temperature for the Mg–Ni–10Li–0.2Ce composite. Moreover, in the first hydrogen cycling the polymorphic phase transition from orthorhombic to hexagonal structure and the melting of $LiBH_4$ are clearly identified [33].

Previous to the kinetic study, stable rates and capacities were attained through hydrogen cycling at 350 °C as shown in Fig. 5(A) and (B). For both composites, the hydrogen absorption rates increase with the successive absorption/desorption cycles and reach the stability after four and three cycles, respectively. It is also noticed that their hydrogen capacities are relatively constant through the hydrogen cycling. Furthermore, after the first cycle the hydrogen capacities are close to those reached the equilibrium conditions of 7.0 wt% H and 6.7 wt% H for Mg–Ni–10Li and Mg–Ni–10Li–0.2Ce composites, respectively.

Fig. 6 shows the non-isothermal behavior of the composites under hydrogen atmosphere after activation. During hydrogen absorption at 2.5 MPa, a sharp exothermic peak attributed to the MgH_2 formation is observed in both composites. This is in agreement with the PXRD shown in Fig. 1(b) (Section 3.1) where the unique detected hydride phase is MgH_2. The absence of the endothermic peaks corresponding to the polymorphic transition and melting of $LiBH_4$ [33] evidences its total decomposition during the activation of the samples. It can be noticed that the hydrogen cycling does not considerable change the absorption behavior of the composites since the rates of hydrogen uptake are alike to those exhibited by the as-milled composites (see Fig. 4). On the other hand, a remarkable reduction in 100 °C is observed for the starting temperature of hydrogen desorption. It suggests that the hydrogen cycling modifies the subsequent reactivity to hydrogen of the composites.

Fig. 7 depicts the hydrogen sorption curves of the composites at 225 and 250 °C where the effect of $CeCl_3$ is clearly noticed.

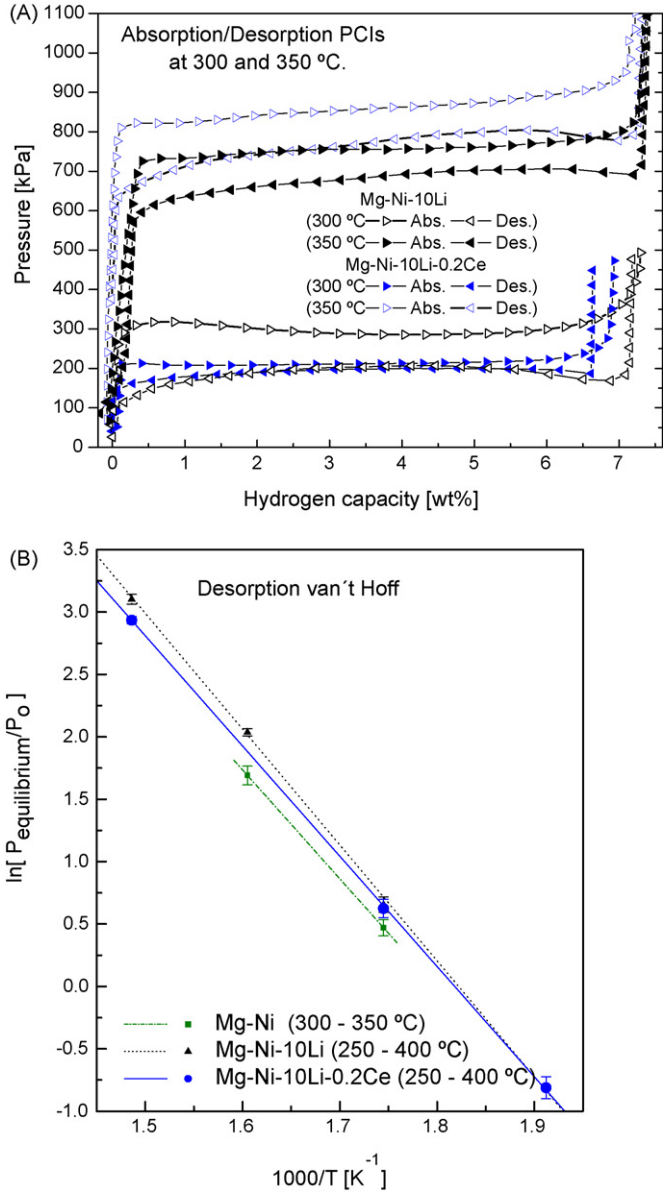

Fig. 3. (A) Pressure-composition isotherm (PCI) curves of Mg–Ni–10Li and Mg–Ni–10Li–0.2Ce composites at 300 and 350 °C; (B) desorption van't Hoff plots for Mg–Ni, Mg–Ni–10Li and Mg–Ni–10Li–0.2Ce composites determined from PCIs in the range of temperature from 250 to 400 °C.

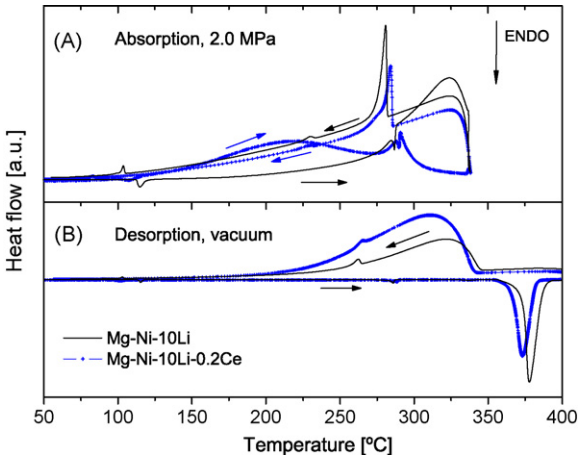

Fig. 4. Comparison of hydrogen absorption/desorption reactions for Mg–Ni–10Li and Mg–Ni–10Li–0.2Ce composites in the HP-DSC equipment. (A) Absorption at 2.0 MPa, heating/cooling rate of 5 K min^{-1} and keeping at 350 °C for 0.5 h. (B) Desorption under vacuum, heating/cooling rate of 5 K min^{-1} up to 400 °C.

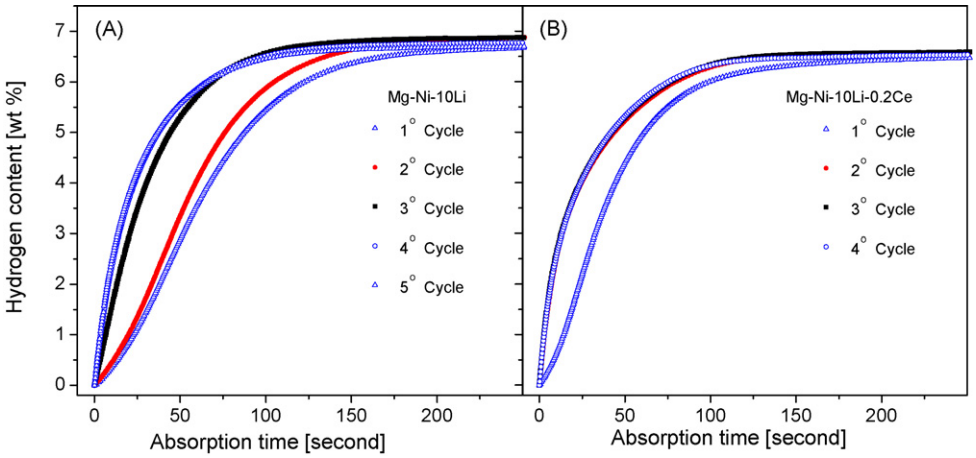

Fig. 5. Activation of the (A) Mg–Ni–10Li and (B) Mg–Ni–10Li–0.2Ce composites through successive hydrogen absorption cycles at 350 °C and 2.5 MPa of H_2.

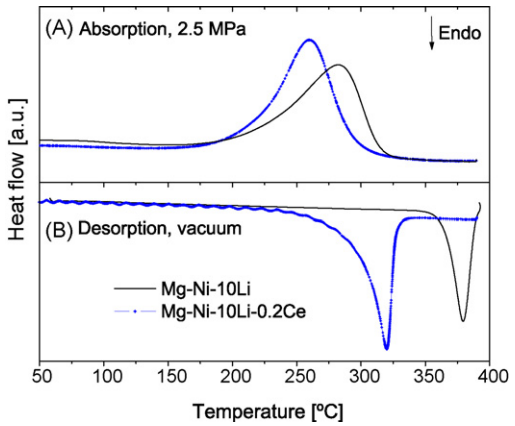

Fig. 6. HP-DSC for Mg–Ni–10Li and Mg–Ni–10Li–0.2Ce composites after cycling: (A) absorption at 2.5 MPa; (B) desorption under vacuum, heating rate of 5 °C min^{-1}.

In the case of the hydrogen uptake, Fig. 7(A), Mg–Ni–10Li–0.2Ce presented faster rates than Mg–Ni–10Li. As seen, Mg–Ni–10Li composite reaches 4.9 wt% H at 225 °C (final capacity of 6.7 wt% H in 50 min – curve (a)) and 6.3 wt% H at 250 °C (final capacity of 6.7 wt% H in 23 min – curve (b)) in 600 s. On the other hand, Mg–Ni–10Li–0.2Ce composite achieves 4.9 wt% H at 225 °C in 425 s (final capacity of 6.5 wt% H in 35 min – curve (c)) and 6.3 wt% H at 250 °C in 330 s (final capacity of 6.6 wt% H in 11 min – curve (d)). This improvement on the absorption kinetic characteristics agree well with the beneficial effect of Ni and Ce on the hydrogen absorption rate and activation properties of Mg-based material reported by Wang et al. [34].

The dehydriding rate curves of Mg–Ni–10Li and Mg–Ni–10Li–0.2Ce composites are shown in Fig. 7(B). At 300 °C, Mg–Ni–10Li–0.2Ce desorbs 4.0 wt% H in 84 min (final capacity of 4.5 wt% H in 2 h – curve (d)), but Mg–Ni–10Li just releases 0.45 wt% H in the same period of time (final capacity of 0.75 wt% H in 2 h and 20 min – curve (b)). As can be clearly noticed, the hydrogen desorption kinetics is markedly precluded by the temperature decrease. However, the Mg–Ni–10Li–0.2Ce composite desorbs hydrogen at 225 °C (0.65 wt% H in 2 h – curve (c)), whereas the Mg–Ni–10Li composite does not (curve (a)). Hence, Mg–Ni–10Li–0.2Ce presents faster desorption rates than Mg–Ni–10Li at lower hydrogen release temperatures, which is in accordance with the non–isothermal desorption behavior of the composites observed in Fig. 6(B).

In view of the results, the Mg–Ni–10Li–0.2Ce composite clearly has superior sorption and cycling properties than the Mg–Ni–10Li composite. Considering that the hydrogen sorption processes occur practically at the same driving force (same equilibrium pressures – Fig. 3), the observed enhancement on the sorption rates is due to kinetic factors.

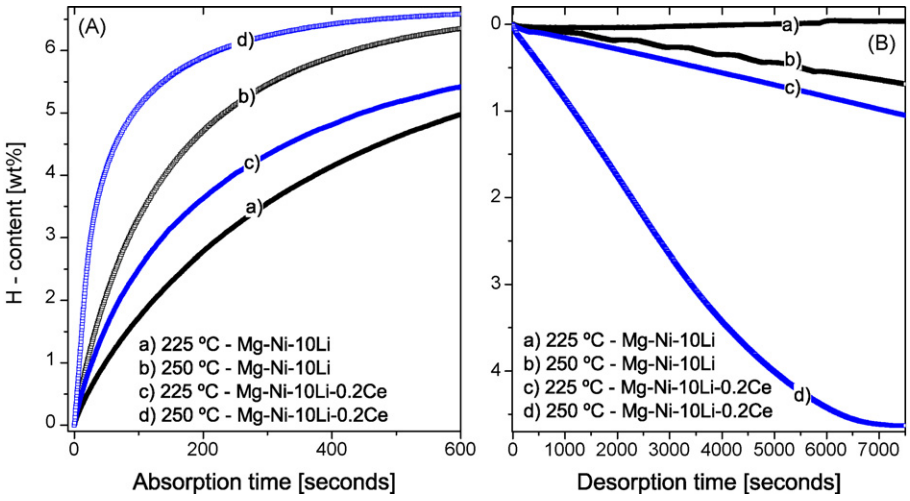

Fig. 7. Comparison of the (A) absorption and (B) desorption kinetics for Mg–Ni–10Li and Mg–Ni–10Li–0.2Ce at 225 and 250 °C under 2.5 MPa of hydrogen pressure for absorption and vacuum for desorption.

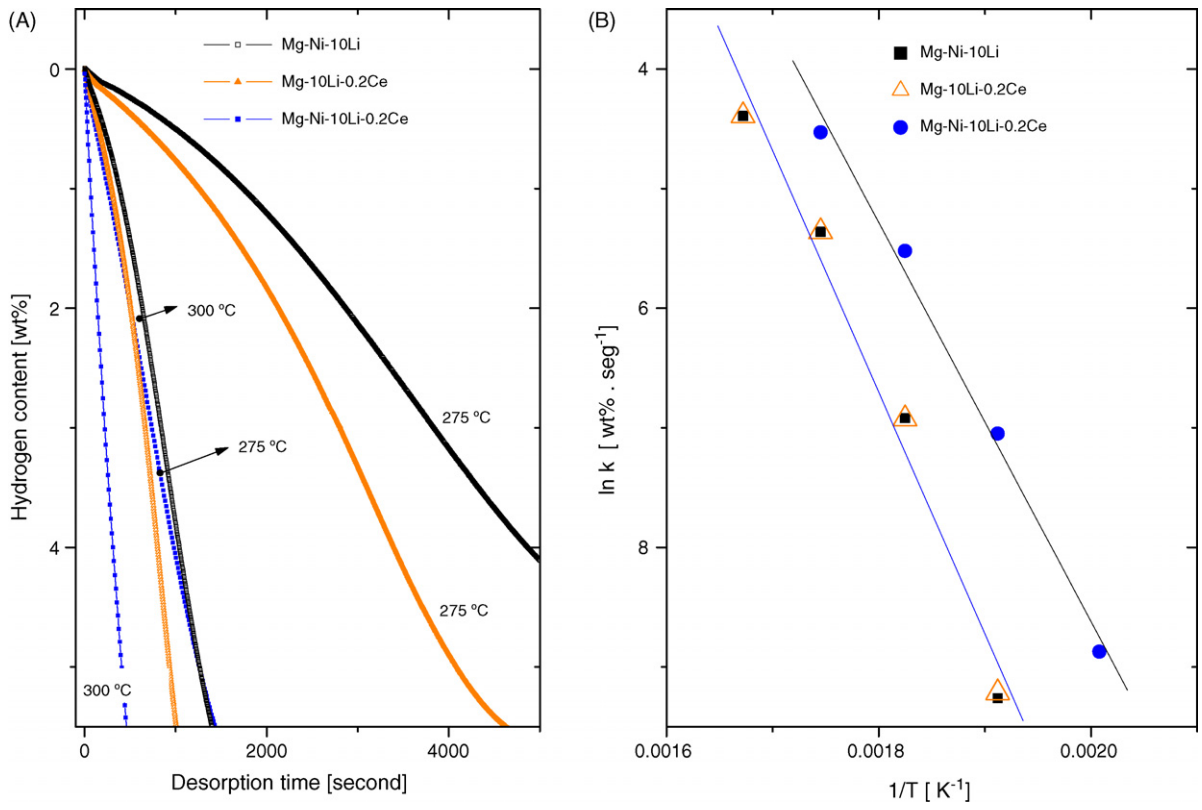

Fig. 8. (A) Comparison of the desorption kinetics for Mg–Ni–10Li, Mg–10Li–0.2Ce and Mg–Ni–10Li–0.2Ce at 275 and 300 °C under vacuum. (B) Arrhenius plot for Mg–Ni–10Li, Mg–10Li–0.2Ce and Mg–Ni–10Li–0.2Ce in the temperature range of 250–325 °C.

3.4. Hydriding–dehydriding: catalytic role of $MgNi_3B_2$ and $CeCl_3$

3.4.1. Activation energy of the desorption process

Fig. 8(A) shows a comparison of the hydrogen desorbed fraction of Mg–Ni–10Li, Mg–10Li–0.2Ce and Mg–Ni–10Li–0.2Ce composites at 275 and 250 °C under vacuum as a function of time. As seen, it is clear that the presence of $CeCl_3$ increases the hydrogen release rates. In order to describe the observed dehydrogenation kinetic behavior, the average desorption rates in the range of 1 wt% H to 4–5 wt% H were calculated. Arrhenius treatment of the rate constant (k) expressed as wt% H per second yields a notable difference among the apparent activation energy (E_a) of the composites (Fig. 8(B)). The addition of $CeCl_3$ to Mg–Ni–10Li decreases the E_a from 171 ± 18 to 139 ± 18 kJ mol^{-1}. On the other hand, the Mg–10Li–0.2Ce composite has the same E_a as Mg–Ni–10Li, suggesting that $CeCl_3$ or $MgNi_3B_2$ has similar contribution on the kinetic behavior of the composites. However, the presence of both $CeCl_3$ and $MgNi_3B_2$ renders a further improvement on the kinetic performance of Mg–Ni–10Li–0.2Ce.

3.4.2. Mg–Ni–Li interactions

In order to understand the reactions between Mg, Ni and $LiBH_4$ during heating, DSC (Fig. 9(A)) and PXRD (Fig. 9(B)) studies on as-milled Mg–Ni–10Li composite were performed. It can be observed that the endothermic events corresponding to the phase transition (107 °C) and melting (277 °C) of $LiBH_4$ (Fig. 9(A) curve (a)) are not affected as Mg–Ni–10Li composite (Fig. 9(A) curve (b)) is heated.

Fig. 9(B) shows the PXRD pattern of the as-milled Mg–Ni–10Li composite heated up to 350 °C keeping them at this temperature for 5 h in vacuum atmosphere. The formation of Mg_2Ni and $MgNi_3B_2$ is clearly identified as well as the simultaneous presence of residual Mg and Ni. Although at temperatures below 300 °C the intermetallic phase Mg_2Ni is formed [35], the melting temperature of $LiBH_4$ does not suffer any change in the presence of Mg_2Ni (Fig. 9(A) – curve (b)). Moreover, above ~330 °C the $LiBH_4$ starts to decompose according to the reaction: $LiBH_4 \rightarrow LiH + B + (3/2)H_2$ [33,36], providing free B which reacts with Ni and Mg or with Mg_2Ni and Ni for the $MgNi_3B_2$ formation. The poor contacting between Mg and Ni and/or the partial decomposition of $LiBH_4$ might account for the detected free Ni which suggests that $MgNi_3B_2$ was partially formed during heating under vacuum. After hydrogen cycling the detected phases in the Mg–Ni–10Li composite are $MgNi_3B_2$

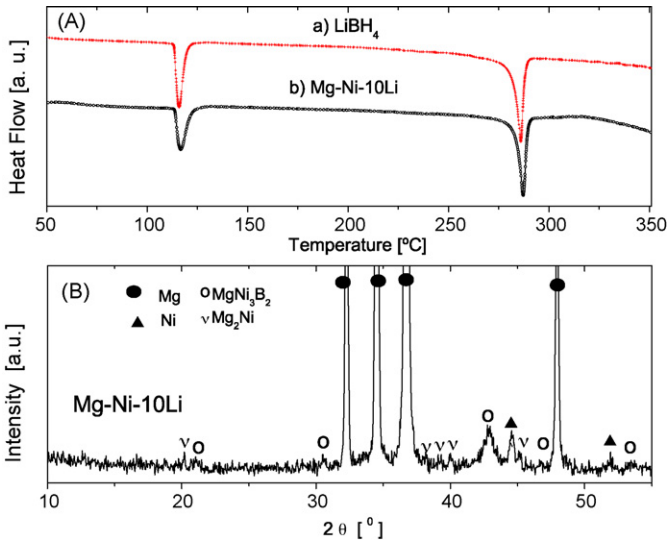

Fig. 9. (A) DSC curves of (a) $LiBH_4$ and as-milled and (b) Mg–Ni–10Li. (B) Powder X-ray diffraction pattern for as-milled Mg–Ni–10Li ramped at 5 °C min^{-1} from room temperature to 350 °C and maintained at 350 °C for 5 h in vacuum atmosphere.

and MgH_2 [27]. Therefore, the formation of $MgNi_3B_2$ starts during heating under vacuum and is totally accomplished upon hydriding as $LiBH_4$ completely decomposes. This is in agreement with the HP-DSC analysis (Fig. 6(A) and (B) – Section 3.3). Once the irreversible phase $MgNi_3B_2$ is formed it operates as catalyst for the formation/decomposition of MgH_2.

3.4.3. Mg–Li–Ce interactions

To that extent the presence of $CeCl_3$ plays a key role in the improvement of the sorption behavior of the Mg–Ni–10Li–0.2Ce composite mainly in the desorption kinetics (see Fig. 8). However, in the PXRD of the samples after hydriding/dehydrigding (Fig. 1(b) and (c)) reflections coming from metallic Ce or any Ce compound have not been detected. Hence, in order to elucidate the actual catalytic effect of $CeCl_3$ in this section the interactions among Mg, $LiBH_4$ and $CeCl_3$ are analyzed. Fig. 10 shows the (A) DSC profiles of $LiBH_4$ and as-milled Mg–Ni–10Li–0.2Ce, Mg–10Li–0.2Ce, Mg–50Li–Ce and Li–Ce ($3LiBH_4$–$CeCl_3$ mixture milled for 6 h), and (B) de PXRD patterns for as-milled Mg–Ni–10Li–0.2Ce, Mg–10Li–0.2Ce and Mg–50Li–Ce heated up to 350 °C keeping them at this temperature for 5 h in vacuum atmosphere.

Three endothermic events are clearly noticed when $CeCl_3$ is present (Fig. 10 – curves (b), (c) and (d)). Two thermal events occur at slightly lower temperature than the phase transition and melting of $LiBH_4$. A third thermal event (marked by a blue arrow) can be associated with the formation during heating of an intermediate phase which involves $LiBH_4$ and $CeCl_3$ interaction, which decomposes at around 255 °C. This is supported by the DSC profile of a $3LiBH_4$–$CeCl_3$ mixture milled for 6 h (Fig. 10 curve (e)), in which the endothermic event at 255 °C is owing to the decomposition of $Ce(BH_4)_3$ formed during the milling process [37]. In the PXRD patterns of Mg–Ni–10Li–0.2Ce (Fig. 10 (B) curve (a)) as well as Mg–Ni–10Li (Fig. 9(B)), Mg, Mg_2Ni, $MgNi_3B_2$ and Ni are detected. It seems that Mg, Ce and Ni do not form any reported phase [34,38–40]. The Mg–50Li–Ce composite (Fig. 10(B) pattern

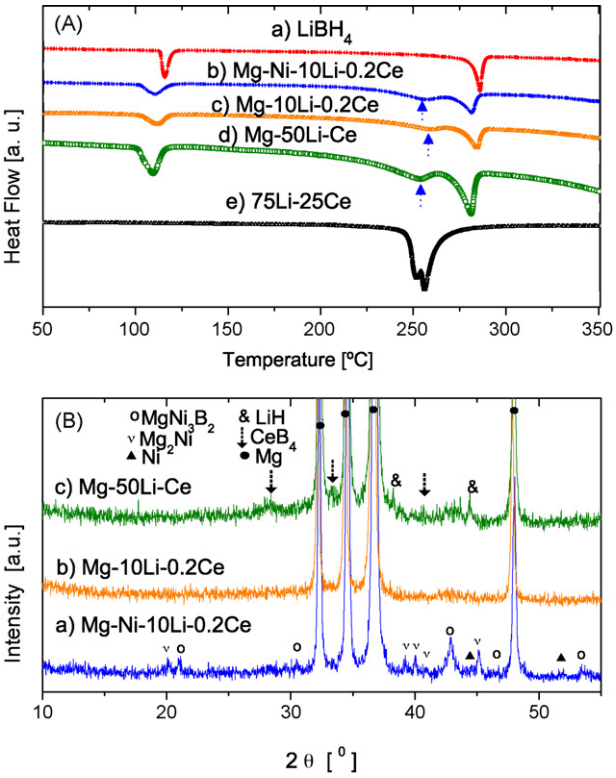

Fig. 10. (A) DSC curves of (a) $LiBH_4$ and as-milled (b) Mg–Ni–10Li–0.2Ce, (c) Mg–10Li–0.2Ce, (d) Mg–50Li–Ce and (e) Li–Ce ($3LiBH_4$–$CeCl_3$ mixture milled for 6 h). (B) Powder X-ray diffraction patterns for as-milled (a) Mg–Ni–10Li–0.2Ce, (b) Mg–10Li–0.2Ce and (c) Mg–50Li–Ce ramped at 5 °C min^{-1} from room temperature to 350 °C and maintained at 350 °C for 5 h in Ar vacuum atmosphere.

Table 2
Calculated equilibrium phases at 25 °C under argon atmosphere for different stoichiometric compositions of $CeCl_3$.

Phases	P(Ar) = 0.01 MPa, 0.2 mol% $CeCl_3$		P(Ar) = 0.01 MPa, 1.5 mol% $CeCl_3$	
	Initial composition (mol%)	Final composition (mol%)	Initial composition (mol%)	Final composition (mol%)
Mg	89.8	69.8	50	–
MgH_2	–	15.4	–	40.3
MgB_2	–	4.6	–	9.7
$LiBH_4$	10	–	48.5	23.1
$CeCl_3$	0.2	–	1.5	–
CeB_4	–	0.2	–	1.5
CeB_6	–	–	–	–
CeH_2	–	–	–	–
LiCl	–	0.6	–	4.5
LiH	–	9.4	–	20.9
B	–	–	–	–

Table 3
Calculated equilibrium phases at 25 °C under hydrogen atmosphere for different stoichiometric compositions of $CeCl_3$.

Phases	P(H_2) = 2 MPa, 0.2 mol% $CeCl_3$		P(H_2) = 2 MPa, 1.5 mol% $CeCl_3$	
	Initial composition (mol%)	Final composition (mol%)	Initial composition (mol%)	Final composition (mol%)
Mg	89.8	–	50	–
MgH_2	–	89.8	–	50
MgB_2	–	–	–	–
$LiBH_4$	10	9.4	48.5	44
$CeCl_3$	0.2	–	1.5	–
CeB_4	–	0.15	–	1.13
CeB_6	–	–	–	–
CeH_2	–	0.05	–	0.37
LiCl	–	0.6	–	4.5
LiH	–	–	–	–
B	–	–	–	–

(c)) shows reflections coming from the presence of LiH and indicated with arrows CeB_4, which is the unique specie associated with Ce. As seen, the reflections stemming from Ce compounds do not appear in the XRD patterns of the samples after heating under vacuum (Fig. 10B (a) and (b)) and after hydriding/dehydriding (Fig. 1(b) and (c)). This fact can be associated to the small quantity of the Ce compounds which might not be detectable by XRD and the nature of species such as borides which are commonly amorphous.

In order to analyze the phases resulting from the Mg, $LiBH_4$ and $CeCl_3$ interactions in argon and vacuum atmosphere, calculations based on the principle of Gibbs free energy minimization using the HSC Chemistry software [29] were performed. It is important to mention that the formation of $MgNi_3B_2$ phase as a product of the Mg–Ni–B interaction (Figs. 1, 9(B) and 10(B)) was not considered for the calculation because the thermodynamic data of this ternary specie are not available. Tables 2 and 3 summarize the HSC Chemistry predictions. These tables do not include all the species (as for example: $MgCl_2$(s), HCl(g), Cl_2(g), Ce(s)) taken into account at the time to perform the calculations. According to the thermodynamic calculations performed under low argon pressure (Table 2), CeB_4 is formed from $CeCl_3$ and $LiBH_4$. Concomitantly, the complete $LiBH_4$ decomposition and MgH_2 formation occur. The following reactions describe the processes with their corresponding free energy change (ΔG) calculated at standard temperature and pressure:

$$Mg(s) + H_2(g) \leftrightarrow MgH_2(s) \qquad \Delta G = -36.34\,kJ\,mol^{-1}\,H_2 \tag{1}$$

$$Mg(s) + 2LiBH_4(s) \leftrightarrow MgB_2(s) + 2LiH(s) + 3H_2(g)$$
$$\Delta G = 7.71\,kJ\,mol^{-1}\,H_2 \tag{2}$$

$$4LiBH_4(s) + CeCl_3(s) \leftrightarrow 3LiCl(s) + LiH + CeB_4(s) + 7.5H_2(g)$$
$$\Delta G = -11.54\,kJ\,mol^{-1}\,H_2 \tag{3}$$

Although the equilibrium composition presented in Table 2 shows that Mg should be hydrogenated to MgH_2, this reaction is not favored under the gaseous phase removal (vacuum). Then, it is not expected to detect MgH_2 in the XRD measurements. The ΔG values of the reaction (2) and (3) suggest that $LiBH_4$ consumption is favored via reaction (3) due to $LiBH_4$–$CeCl_3$ interaction. In the case of reaction (2), it is known that MgB_2 formation from Mg–$LiBH_4$ requires overpressure under desorption conditions [41,42] and higher temperatures than 350 °C. However, under the employed experimental conditions it is possible that $LiBH_4$ decomposes following the reaction:

$$LiBH_4(s) \rightarrow LiH(s) + B(s) + 1.5H_2(g) \qquad \Delta G = 37.56\,kJ\,mol^{-1}\,H_2 \tag{4}$$

This reaction is favored under vacuum at high temperature (see Section 3.4.2) [33,36]. Therefore, the $LiBH_4$ decomposition mainly occurs via reaction (4). Moreover, DSC analysis (Fig. 10(A)) and a previous study [37] strongly support the hypothesis that $Ce(BH_4)_3$ is formed as an intermediate of $LiBH_4$–$CeCl_3$ interaction. The evidence presented in Fig. 10(B) curve (c) and the thermodynamic calculations (Table 2) verify that $Ce(BH_4)_3$ decomposition produces CeB_4 under the current experimental conditions.

Upon hydriding reaction thermodynamic calculations predict the following reactions for Mg–Li–Ce system (see Table 3):

$$Mg(s) + H_2(g) \leftrightarrow MgH_2(s) \qquad \Delta G = -36.34\,kJ\,mol^{-1}\,H_2 \tag{5}$$

$$3LiBH_4(s) + CeCl_3(s) \leftrightarrow 3LiCl(s) + 0.75CeB_4(s) + 0.25CeH_2(s)$$
$$+ 5.75H_2(g) \qquad \Delta G = -16.47\,kJ\,mol^{-1}\,H_2 \tag{6}$$

Reaction (5) is in accordance with the PXRD analysis after hydriding/dehydriding shown in Fig. 1(b) and (c) in which the presence of MgH_2 and Mg is clearly detected. This reversible hydriding/dehydriding reaction is the main focus of this investigation since Mg is the phase which is in the highest proportion and besides, as seen in Section 3.2, the thermodynamic behavior of the studied composites correspond to MgH_2. According to reaction (6), the interaction between $LiBH_4$ and $CeCl_3$ would lead to the formation of CeH_2. In our previous work [37], the dehydriding of $Ce(BH_4)_3$ leads to the formation of CeH_2 and a boride compound and its subsequent hydrogen absorption is not complete (28% of total hydrogen capacity). Taking into account the thermodynamic calculations and the experimental conditions used in the present study, it is not expected to observe reversibility from the reaction (6) through $Ce(BH_4)_3$ as intermediate due to kinetic restrictions.

Therefore, from the calculations performed in equilibrium conditions and the experimental evidence it is possible to describe the processes occurring when the Mg–Li–Ce system is heated. $LiBH_4$ partially decomposes through the reactions (3) and (4) leading to the formation of CeB_4, LiCl, LiH and B as condensate phases. Further thermal treatment under high hydrogen pressure induces hydriding of Mg to MgH_2 and complete decomposition of $LiBH_4$. It is believed that the formation and decomposition of the intermediate phase $Ce(BH_4)_3$ favors the dispersion of nanosize CeB_4 on the MgH_2 surface. The formation of the cerium borohydride during heating from a $3LiBH_4$–$CeCl_3$ mixture milled for 1 h has been experimentally demonstrated by our group [37]. Fang et al. [43] have observed a similar behavior associated with the in situ formation and rapid decomposition of the intermediate $Ti(BH_4)_3$ and the subsequent formation of Ti compound during heating. Moreover, Kostka et al. [44] have reported the formation of the intermediate phase $La(BH_4)_x$ when $LiBH_4$ was ball-milled with $LaCl_3$. Thus, the intermediate cerium borohydride decomposes at lower temperature than $LiBH_4$ providing free boron for the complete formation of $MgNi_3B_2$ and Ce for the formation of the CeB_4. The presence of CeH_2 under vacuum or hydrogen atmosphere dependents on the stoichiometric ratio between $LiBH_4$–$CeCl_3$. In the case of the analyzed composites the stoichiometric $LiBH_4$–$CeCl_3$ ratio does not favor the CeH_2 formation. Based on the calculations and the experimental evidence (Fig. 10(B) pattern (a)), it is possible to conclude that along with the formation of $MgNi_3B_2$ similar reactions are involved as the Mg–Ni–10Li–0.2Ce composite is first heated under vacuum and then cycled in hydrogen.

In the Mg–Ni–10Li–0.2Ce composite are present both $MgNi_3B_2$ and CeB_4. The irreversible ternary phase $MgNi_3B_2$ formed in Mg–Ni–10Li and Mg–Ni–10Li–0.2Ce serves as a reaction pathway, improving the diffusion of hydrogen through the formed magnesium hydride [27]. The catalytic activity of CeB_4 is conferred by two characteristics. First, the high valence state of Ce in the CeB_4 structure which increases the catalytic activity because more electrons are exchanged during the catalytic reaction [45,46]. Second, the high affinity of Ce for hydrogen since it can form cerium hydrides such as CeH_2 [45–48]. These characteristics would facilitate the nucleation process, accelerating the incubation period as Mg uptakes and releases hydrogen [46]. As seen, both compounds play a catalytic role in the formation–decomposition of MgH_2. Therefore, the further enhancement in the sorption kinetic characteristics of the Mg–Ni–10Li–0.2Ce composite is attributed to the synergetic effect of both $MgNi_3B_2$ and CeB_4 catalytic phases.

3.5. Conclusions

The Mg–Ni–10Li–0.2Ce composite prepared by short times of ball milling in argon atmosphere has better hydrogen sorption performance than Mg–Ni–10Li. This composite absorbs 6.30 wt% H at 300 °C in about 300 s and released hydrogen at a lower temperature

(225 °C) than Mg–Ni–10Li. According to the experimental results, the Mg–Ni–10Li and Mg–Ni–10Li–0.2Ce composites do not present any relevant differences regarding microstructure and morphology, and their thermodynamic behaviors correspond to MgH_2. During heating, the interaction between $LiBH_4$ and $CeCl_3$ results in the intermediate cerium borohydride which ease the subsequent formation of $MgNi_3B_2$ and provides CeB_4 as final product. Both $MgNi_3B_2$ and CeB_4 have catalytic effects on MgH_2 resulting in the enhanced sorption kinetics of the Mg–Ni–10Li–0.2Ce composite.

Acknowledgments

The authors thank CONICET, ANPCyT and Balseiro Institute (National University of Cuyo) for financial support to carry out this work.

References

[1] S. Satyapal, J. Petrovic, G. Thomas, Sci. Am. 296 (2007) 80–87.
[2] A. Zaluska, L. Zaluski, J.O. Ström-Olsen, Appl. Phys. A 72 (2007) 157–165.
[3] A. Zaluska, L. Zaluski, J.O. Ström-Olsen, J. Alloys Compd. 253/254 (1997) 70–79.
[4] H. Imamura, K. Masanari, M. Kusuhara, H. Katsumoto, T. Sumi, Y. Sakata, J. Alloys Compd. 386 (2005) 211–216.
[5] M. Zhu, H. Wang, L.Z. Ouyang, M.Q. Zeng, Int. J. Hydrogen Energy 31 (2006) 251–257.
[6] W. Grochala, P. Edwards, Chem. Rev. 104 (2004) 1283–1316.
[7] C. Suryanarayana, Prog. Mater. Sci. 46 (2001) 1–184.
[8] A. Zaluska, L. Zaluski, J.O. Ström-Olsen, J. Alloys Compd. 289 (1999) 197–206.
[9] G. Liang, J. Huot, S. Boily, A.V. Neste, R. Schulz, J. Alloys Compd. 292 (1999) 247–252.
[10] Z. Dehouche, J. Goyette, T.K. Bose, J. Huot, R. Schulz, Nano Lett. 1 (2001) 175–178.
[11] W. Oelerich, T. Klassen, R. Bormann, J. Alloys Compd. 315 (2001) 237–242.
[12] J.F. Pelletier, J. Huot, M. Sutton, R. Schulz, A.R. Sandy, L.B. Lurio, S.G. Mochrie, J. Phys. Rev. B 63 (2001) 052103.
[13] G. Barkhordarian, T. Klassen, R. Bormann, Scr. Mater. 49 (2003) 213–217.
[14] G. Liang, J. Alloys Compd. 370 (2004) 123–128.
[15] J.J. Vajo, F. Mertens, C.C. Ahn, R.C. Bowman, B. Fultz, J. Phys. Chem. B 108 (2004) 13977–13983.
[16] N. Hanada, T. Ichikawa, H. Fujii, J. Phys. Chem. B 109 (2005) 7188–7194.
[17] G. Barkhordarian, T. Klassen, R. Bormann, J. Phys. Chem. B 110 (2006) 11020–11024.
[18] X. Yao, C. Wu, A. Du, G.Q. Lu, H. Cheng, S.C. Smith, J. Zou, Y. He, J. Phys. Chem. B 110 (2006) 11697–11703.
[19] K.F. Aguey-Zinsou, J.R. Ares Fernandez, T. Klassen, R. Bormann, Mater. Res. Bull. 41 (2006) 1118–1126.
[20] S.-A. Jin, J.-H. Shim, P.-J. Ahn, Y.W. Cho, K.-W. Yi, Acta Mater. 55 (2007) 5073–5079.
[21] L. Xie, Y. Liu, Y.T. Wang, J. Zheng, X.G. Li, Acta Mater. 55 (2007) 4585–4591.
[22] S.-A. Jin, J.-H. Shim, P.-J. Ahn, Y.W. Cho, K.-W. Yi, J. Power Sources 172 (2007) 859–862.
[23] Y.J. Choi, J. Lu, H.Y. Sohn, Z.Z. Fang, J. Power Sources 180 (2008) 491–497.
[24] J.A. Puszkiel, P. Larochette Arneodo, F.C. Gennari, J. Power Sources 186 (2008) 185–193.
[25] S.R. Johnson, P.A. Anderson, P.P. Edwards, I. Gameson, J.W. Prendergast, M. Al-Mamouri, D. Book, I. Rex Harris, J.D. Speight, A. Walton, Chem. Commun. 22 (2005) 2823–2825.
[26] J.F. Mao, Z. Wu, T.J. Chen, B.C. Weng, N.X. Xu, T.S. Huang, Z.P. Guo, H.K. Liu, D.M. Grant, G.S. Walker, X.B. Yu, J. Phys. Chem. C 111 (2007) 12495–12498.
[27] J.A. Puszkiel, F.C. Gennari, Scr. Mater. 60 (2009) 667–670.
[28] G.D. Meyer, S. Rodríguez, F. Castro, G. Fernández, Proceedings of the 11th World Energy Conference, Stuttgart, Germany, 23–29, June, 1996, pp. 1293–1298.
[29] Outokumpu HSC Chemistry for Windows, version 6.0, Outokumpu Research Oy, Pori, Findland, 2009.
[30] J.J. Vajo, F. Mertens, C. Ahn, R. Bowman, B. Fultz, J. Phys. Chem. B 108 (2004) 13977–13983.
[31] A.S. Pedersen, J. Kjoller, B. Larsen, B. Vigeholm, Int. J. Hydrogen Energy 8 (1983) 205–211.
[32] J.F. Stampfer, C.E. Holley, J.F. Suttle, J Am Chem. Soc. 82 (7) (1960) 3504–3508.
[33] S. Orimo, Y. Nakamori, G. Kitahara, K. Miwa, N. Ohba, S. Towata, A. Züttel, J. Alloys Compd. 404–406 (2005) 427–430.
[34] X.L. Wang, J.P. Tu, C.H. Wang, X.B. Zhang, C.P. Chen, X.B. Zhao, J. Power Sources 159 (2006) 163–166.
[35] F.C. Gennari, M.R. Esquivel, J. Alloys Compd. 459 (2008) 425–432.
[36] A. Züttel, P. Wenger, S. Rentsch, P. Sudan, Ph Mauron, Ch. Emmenegger, J. Power Sources 118 (2003) 1–7.
[37] F.C Gennari, M.R. Esquivel, J. Alloys Compd. 485 (2009) L47–L51.
[38] M. Pezat, B. Darriet, P. Hagenmuller, J. Less-Common Met. 74 (1980) 427–434.
[39] E. Ivanov, I. Konstanchuk, A. Stepanov, V. Boldirev, J. Less-Common Met. 131 (1987) 25–29.
[40] M. El Hammioui, L. Belkbir, J. Alloys Compd. 202 (1993) 199–202.
[41] U. Bösenberg, S. Doppiu, L. Mosegaard, G. Barkhordarian, N. Eigen, A. Borgschulte, T. Jensen, Y. Cerenius, O. Gutfleisch, T. Klassen, Acta Mater. 55 (2007) 3951–3958.
[42] T. Nakagawa, T. Ichikawa, N. Hanada, Y. Kojima, H. Fujii, J. Alloys Compd. 446/447 (2007) 306–309.
[43] Z.Z. Fang, L.P. Ma, X.D. Kang, P.J. Wang, M.H. Cheng, Appl. Phys. Lett. 94 (2009), 044104 (1–4).
[44] J. Kostka, W. Lohstroh, M. Fichtner, H. Hahn, J. Phys. Chem. C 111 (2007) 14026–14029.
[45] Y.M. Goryachev, B.A. Kovenskaya, E.M. Dudnik, E.N. Severyanina, B.G. Arabei, Zh. Struk. Khim. 16 (1975) 1036.
[46] G. Barkhordarian, T. Klassen, R. Bormann, J. Phys. Chem. B 11020 (2006) 11020–11024.
[47] M. El Hammioui, L. Belkbir, J. Alloys Compd. 202 (1993) 183–199.
[48] S.D. Jackson, G.J. Kelly, E.M. Vass, J. Alloys Compd. 459 (2008) 113–117.